nature communications

Article

https://doi.org/10.1038/s41467-026-76733-8

Heterogeneously integrated photonic terahertz transmitter on thin-film lithium niobate

Received: 29 November 2025

Accepted: 31 July 2026

Published online: 14 August 2026

Check for updates

Luyu Wang[1,2,5], Hanke Feng[3,5], Liga Bai[4,5], Zhouze Zhang[1,5], Zhe Ding[4], Yifan Wu[3], Linze Li[1,2], Dingran Gu[1], Tianyu Long[1,2], Lu Zhang[4], Xianbin Yu[4], Zhidong Lyu[4] ✉, Cheng Wang[3] ✉ & Baile Chen[1] ✉

Terahertz (THz) communication unlocks massive capacity for future data-intensive networks. While photonics-based THz systems offer broad bandwidths, their reliance on discrete optical assemblies dictates substantial coupling losses and bulky footprints. Achieving complete on-chip integration without degrading the bandwidth or efficiency of discrete optoelectronic components remains a central challenge. Here, we demonstrate an integrated photonic THz transmitter by heterogeneously bonding an InP-based uni-traveling-carrier photodiode (UTC-PD) to a thin-film lithium niobate (TFLN) modulator chip. This architecture successfully merges TFLN's excellent electro-optic response with robust III-V THz generation, featuring an integrated photodiode with a benchmark 3-dB bandwidth of 240 GHz and 0.67 A/W internal responsivity. In sub-THz wireless links, the transmitter delivers 40 Gbit/s at 150 GHz and 32 Gbit/s at 200 GHz using NRZ or PAM4 formats, establishing a scalable pathway for next-generation wireless interconnects.

The explosive growth of data-intensive applications in artificial intelligence (AI) and immersive media is pushing wireless networks to scale their capacity, latency, and interconnectivity[1,2]. To address this demand, the terahertz (THz) band (0.1–10 THz) has emerged as a promising solution for ultrabroad bandwidth wireless in 6G and beyond networks[3,4]. Within this framework, THz transmitters, responsible for generating THz carrier signals and modulating baseband data onto the carrier, play a critical role[5,6]. Over the years, conventional electronic schemes based on solid-state multiplier chains and mixers have been the primary method for THz generation. However, these approaches are fundamentally constrained by the nonlinear nature of harmonic up-conversion and limited bandwidth of analog electronics, which limit their applicability in broadband and power-efficient THz links[7,8].

Photonics-assisted approaches have proven to be a compelling alternative, offering sufficient bandwidth, low phase noise, and flexible frequency tunability[9–11]. In such systems, high-speed photodiodes (PD) play a central role through optical heterodyning, in which two narrow-linewidth lasers generate a THz beating signal that is converted into the THz domain without transistor-related bottlenecks[6,10]. Among various PD technologies, the uni-traveling-carrier photodiode (UTC-PD)[12] is characterized by its electron-dominated transport mechanism. By utilizing only electrons as the active carriers, UTC-PDs can achieve ultra-high bandwidth while maintaining a linear response even under high-power injection, establishing them as an effective choice for broadband THz emitters[13–15]. Leveraging these capabilities, UTC-PDs have recently enabled ultra-high-speed wireless links exceeding 100 Gbit/s in the sub-THz regime[10,16,17]. However, most of such systems still rely on discrete optoelectronic components that typically necessitate bulky supporting equipment, including high-power lasers and multiple optical amplifiers, to compensate for the substantial coupling and transmission losses[18]. Such configurations severely limit the scalability and flexibility required

[1]School of Information Science and Technology, ShanghaiTech University, Shanghai, China. [2]Fastphide Photonics, Shanghai, China. [3]Department of Electrical Engineering & State Key Laboratory of Terahertz and Millimeter Waves, City University of Hong Kong, Hong Kong, China. [4]College of Information Science and Electronic Engineering, Zhejiang University, Hangzhou, China. [5]These authors contributed equally: Luyu Wang, Hanke Feng, Liga Bai, Zhouze Zhang. ✉e-mail: zdlyu@zju.edu.cn; cwang257@cityu.edu.hk; chenbl@shanghaitech.edu.cn

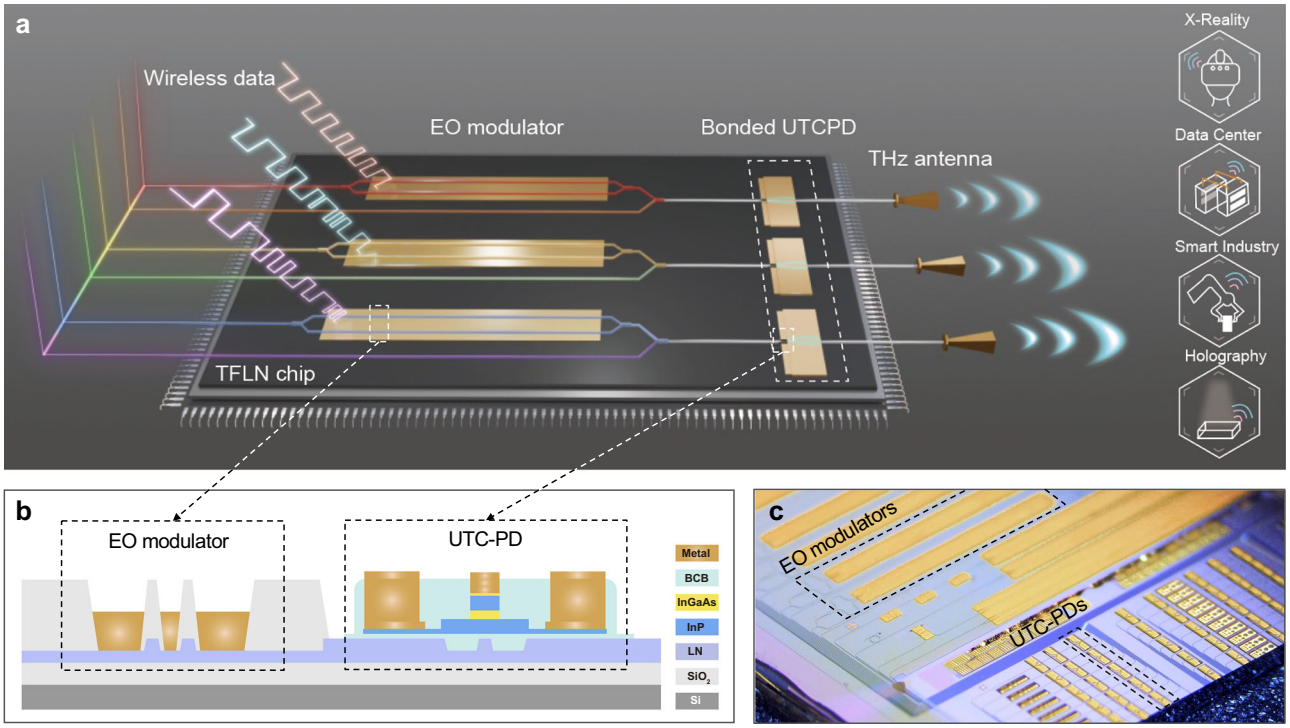


Fig. 1 | Heterogeneously integrated TFLN-based photonic THz transmitter. **a** Schematic illustration of the THz transmitter chip and its application scenario. A centralized multi-wavelength source is distributed to transmitter chips, where the EO modulator imprints baseband data onto an optical tone, and the bonded UTC-PD converts the heterodyne beating of the optical signals into tunable THz carriers. **b** Cross-sectional schematic of the modulator and UTC-PD regions. **c** Optical micrograph of a fabricated chip.

for large-scale deployment in future 6G networks, necessitating the on-chip integration of UTC-PDs with other essential photonic components to develop compact, energy-efficient THz front-ends.

While monolithic integration on Indium Phosphide (InP) platforms —which aims to consolidate lasers, modulators, and photodetectors onto a single chip—has been proposed for THz transmitters[9,19], practical communication demonstrations using this intrinsic approach remain hindered by fundamental bottlenecks. Specifically, conflicting epitaxial requirements for different active components severely compromise the overall performance. Moreover, InP platforms face intrinsic physical limitations, including pronounced propagation losses from free-carrier absorption[20] and a nonlinear electro-optic response that degrades high-frequency modulation fidelity[21].

To overcome these constraints, heterogeneous integration offers a path to combine InP-based components with low-loss, broadband photonic platforms that support advanced modulation and signal routing[22–24]. Among these platforms, thin-film lithium niobate (TFLN) is particularly attractive due to its strong electro-optic (EO) properties with low optical loss and excellent scalability. These characteristics enable sub-THz EO modulators operating at CMOS-compatible voltages, which facilitate energy-efficient Tb/s data throughput[25,26]. At the same time, the expanding availability of foundry-level processes for TFLN has enabled large-scale integration of diverse low-loss components, providing a promising basis for integrated THz photonics[27–29].

Recent efforts have explored the integration of UTC-PDs with TFLN, including heterogeneously integrated MUTC-PDs on TFLN exhibiting 80 GHz bandwidth and 0.6 A/W responsivity[30], as well as wafer-level InP-TFLN integration reaching 140 GHz bandwidth and 0.4 A/W responsivity[31]. However, the performance scaling in these works highlights a fundamental physical trade-off inherent in high-speed photodetectors: achieving a higher bandwidth requires a thinner absorption layer and a smaller device footprint to minimize carrier transit time and RC capacitance, which inevitably severely degrades the optical absorption efficiency[32]. While these existing devices have enabled baseband optical communication experiments, their bandwidths still fall short of the requirements for THz communication, and scaling to higher bandwidths inevitably results in a reduction in responsivity. Moreover, the large refractive index contrast between the TFLN waveguide and the III–V layers results in a severe optical mode mismatch, which further compromises the coupling efficiency. Therefore, realizing efficient on-chip THz generation on TFLN demands advanced device architectures capable of simultaneously overcoming the heterogeneous coupling bottleneck while pushing the bandwidth of the PD into the sub-THz regime.

In this work, we address these unmet demands by developing a heterogeneously integrated THz transmitter on the TFLN platform, comprising a high-speed TFLN modulator for data encoding and a 240-GHz bonded InP UTC-PD for THz generation. By utilizing a dual-step matching layer configuration, we achieve efficient optical field coupling between the low-index TFLN waveguide and the InGaAs absorber of the UTC-PD. Combined with a bandgap-engineered epitaxial design, the UTC-PD achieves a 3-dB bandwidth of 240 GHz and an internal responsivity of 0.67 A/W—representing the highest bandwidth-efficiency product among heterogeneously integrated photodiodes to date. System-level performance is demonstrated through sub-THz wireless links, where 40 GBaud NRZ at 150 GHz carrier frequency and 16 GBaud PAM4 at 200 GHz are achieved. This multi-band and multi-format operational versatility confirms that this work provides a scalable hardware foundation for future ultra-broadband photonic-wireless networks.

Results

Chip design and fabrication

Figure 1a presents a schematic of the proposed integrated THz photonic transmitter and its potential application scenarios. The transmitter enables direct on-chip THz generation via optical heterodyning

https://doi.org/10.1038/s41467-026-76733-8

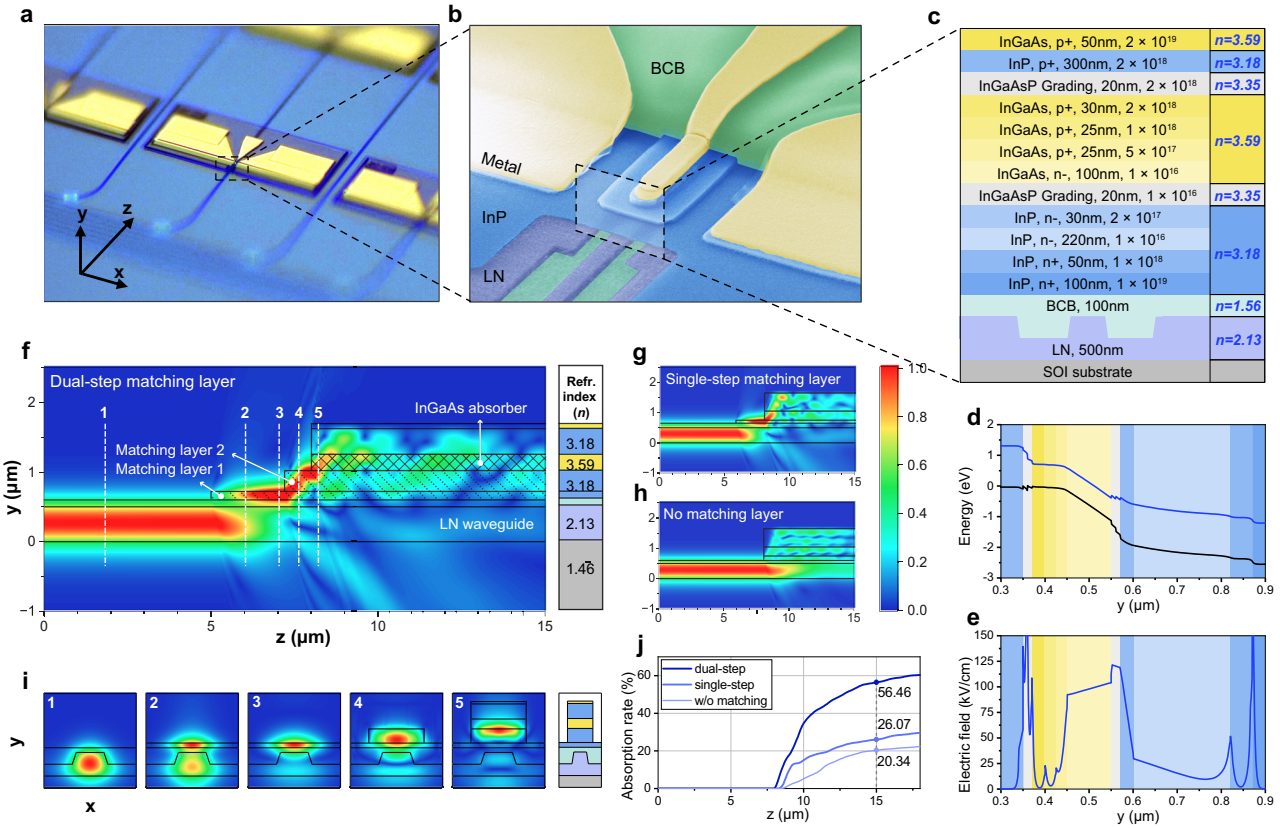


Fig. 2 | Design and fabrication of the heterogeneously integrated UTC-PD. **a** Optical image of the fabricated UTC-PD and the LN waveguide. **b** False-color Scanning electron micrograph (SEM) of the UTC-PD mesa structure. **c** Epitaxial layer design of the InGaAs/InP modified UTC-PD bonded on TFLN, including refractive indices (n). **d** Simulated energy band diagram. **e** Simulated electric field distribution of the UTC-PD under -1 V bias voltage. Simulated optical intensity as light propagates through the UTC-PD with **f** dual-step matching layers(refractive index profile shown in the sidebar) **g** single-step matching layers, and **h** no matching layers. **i** Optical mode profile at different positions along the coupling interface of the dual-step matching structure, corresponding to the white dashed lines 1–5 marked in (**f**). **j** Simulated absorption efficiency as a function of propagation length for dual-step, single-step, and no matching structure.

and data encoding via electro-optic modulation, through the co-integration of high-speed TFLN modulators and heterogeneously bonded UTC-PDs. Specifically, two continuous-wave (CW) laser tones are delivered to each transmitter unit. To support high-linearity signaling for advanced modulation formats (e.g., PAM4), a single sub-carrier (SSC) modulation scheme is adopted. Under this configuration, only one tone is modulated by the EO modulator to encode baseband data, while the other remains unmodulated as an optical local oscillator. These two tones are then combined via a multi-mode interferometer (MMI) coupler and fed into the UTC-PD for photomixing. The generated signal is then directly radiated via a THz antenna for wireless transmission. This scalable scheme is particularly suited for high-capacity, short-range indoor networks serving multiple users, with potential applications spanning extended reality (XR), wireless data center interconnects, smart manufacturing, and holographic communication systems[33–37].

Figure 1b illustrates the cross-section schematics of the co-integrated high-speed EO modulator and UTC-PD within a unified TFLN platform, where the InP epitaxial stack is bonded directly onto the TFLN waveguide layer through a thin (~100 nm) divinylsiloxane-bis-benzocyclobutene (DVS-BCB) adhesive layer[38], ensuring efficient optical coupling and fabrication compatibility. A thick DVS-BCB over-cladding passivates the UTC-PD sidewalls and provides a planar dielectric surface for electrode formation. The resulting non-suspended electrode configuration ensures stable high-frequency performance and improved structural robustness. Detailed fabrication process is discussed in the Methods. The optical image in Fig. 1c shows the compact and scalable chip layout, where dense arrays of EO modulators and heterogeneously integrated UTC-PDs are patterned on a 1 × 1.5 cm^2 TFLN chip. The fabrication flow is fully compatible with wafer-scale processing, enabling scalable integration of complex THz photonic circuits.

The UTC-PD here retains the core active-layer design of our previous epitaxial structure[39] with targeted modifications to enhance responsivity. As shown in the cross-section diagram in Fig. 2c, the epitaxial design incorporates a 180 nm partially depleted $In_{0.53}Ga_{0.47}As$ absorption layer, which enables sufficient optical absorption while maintaining a high internal electric field at the heterojunction interface. To enhance velocity overshoot and suppress carrier accumulation, a 30 nm n-doped InP cliff layer (2 × 10^{17} cm^{-3}) is inserted at the absorption-drift interface. This region locally intensifies the electric field, preventing collapse under high optical injection and maintaining an appropriate electric field within the 220 nm InP collector to support electron transport with overshoot velocity. A 100 nm heavily n-doped InP layer serves as the n-contact. More details are provided in Supplementary Note 2.

Efficient optical coupling between the TFLN waveguide and the III–V photodiode is critical for achieving high responsivity, especially in compact device footprints. However, a key challenge arises from the significant refractive index contrast between LN ($n \approx 2.13$) and the InGaAs absorption layer ($n \approx 3.59$). Without additional matching structures, direct coupling from the LN waveguide into the PD absorption layer demands an extended interaction length, which is incompatible with compact integration[22].

To address this issue, we introduce a dual-step optical mode-matching structure that gradually bridges the refractive index gap

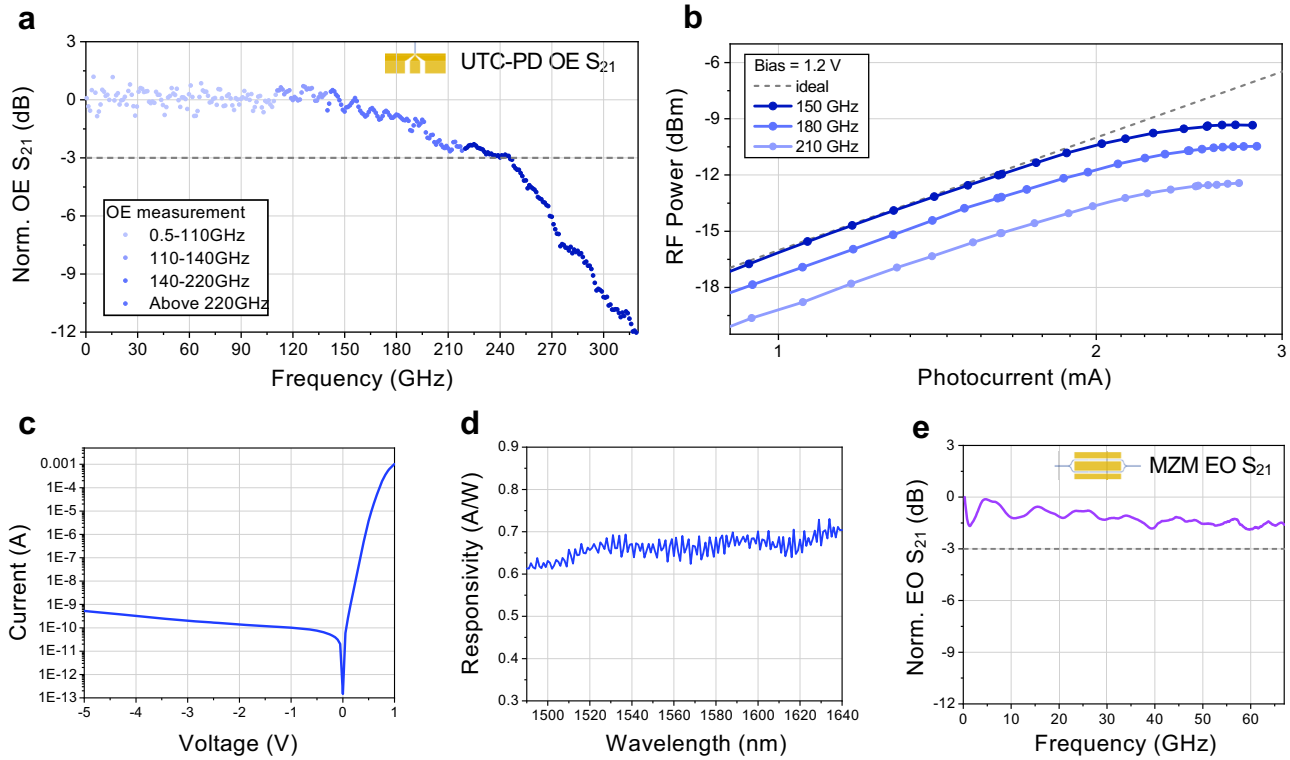


Fig. 3 | Characterization of the integrated UTC-PD and EO modulator. **a** Frequency response of a bonded UTC-PD ($2 \times 7\ \mu m^2$) at 1 mA photocurrent. **b** Measured RF output power as a function of photocurrent at 150, 180, and 210 GHz under −1.2 V bias. **c** Dark current versus bias voltage characteristic of the UTC-PD. **d** Spectral internal responsivity of the UTC-PD from 1490 to 1640 nm. **e** EO S21 responses of the on-chip MZM.

between the underlying LN ($n \approx 2.13$) and InGaAs ($n \approx 3.59$). As evidenced by the false-color SEM image in Fig. 2b and the epitaxial cross-section in Fig. 2c, the InP ($n \approx 3.18$) collector and n-contact region of the UTC-PD are etched into two precisely defined steps. This cascaded morphology creates an intermediate effective-index gradient that enables smooth mode evolution from the TFLN waveguide into the high-index absorber.

To evaluate and optimize this coupling design, finite-difference time-domain (FDTD) simulations were performed. The simulated optical intensity profile (Fig. 2f) serves as a visual guide to delineate the functional role of each step. Specifically, the first step (located between dashed lines 1 and 2 in Fig. 2f), with an etch depth of 100 nm, is designed to match the effective index of the TE mode in the LN waveguide. Its lateral length (2.2 µm) is optimized according to the phase-matching condition for directional coupling. Its lateral length (2.2 µm) is optimized according to the phase-matching condition for directional coupling. The second step (located between dashed lines 3 and 4 in Fig. 2f), etched to a depth of 300 nm and extended by 0.8 µm, accelerates energy transfer into the absorber region while minimizing reflections. Concurrently, the cross-sectional profiles in Fig. 2i (marked 1–5) visually confirm this successive upward migration, culminating in the optical power being predominantly confined within the InGaAs layer (beyond dashed line 5) for high-efficiency absorption.

Compared with devices without (Fig. 2h) or with a single-step matching layer (Fig. 2g), the optical mode in the dual-step design undergoes a faster and more continuous spatial transition within a total coupling length of only 3 µm. Figure 2j shows the simulated absorption efficiency as a function of propagation length. The dual-step design yields a simulated quantum efficiency of 56.46% (responsivity of 0.71 A/W) for an active region length of 7 µm. For comparison, we overlay curves for single-step and no-matching configurations, both of which see significantly slower absorption rate, confirming the critical role of dual-step matching in achieving compact, high-efficiency integration.

UTC-PD characterization

The frequency response of the UTC-PD is characterized using an optical heterodyne system (Methods and Supplementary Note 3), with all measurements conducted in situ on the fully integrated transmitter chip. As shown in Fig. 3a, the fabricated $2 \times 7\ \mu m^2$ PD achieves a 3-dB electrical bandwidth of 240 GHz at a photocurrent of 1 mA. To the best of our knowledge, this represents the highest bandwidth reported thus far for heterogeneously integrated PDs on TFLN platforms. The output power remains broadly uniform from DC to 180 GHz, which is essential for broadband communication as it minimizes amplitude distortion and simplifies digital equalization[40].

To further evaluate the saturation characteristics of the PD, the output RF power is measured directly using a GSG probe and a THz power meter (Methods and Supplementary Note 3) at 150, 180, and 210 GHz, as shown in Fig. 3b. At 150 GHz, the device delivers a peak output RF power of −9.3 dBm at a photocurrent of 2.8 mA. At higher frequencies, the maximum achievable output power decreases, consistent with the device's frequency response roll-off. The achieved output power is sufficient for centimetre- to metre-scale THz links, where sub-milliwatt levels are typically adequate due to focused beams and close transceiver spacing[9,41]. For longer-distance or higher-frequency links, external PAs can be employed to further boost the THz signal.

Figure 3c shows the measured DC current-voltage (I-V) characteristics of the fabricated UTC-PD. At a working reverse bias of −1 V, the dark current remains around 100 pA at room temperature, reflecting high-quality epitaxial growth and effective sidewall passivation achieved through dry etching and surface treatment. Such low leakage current is essential for THz photomixing, as it reduces the shot-noise floor and consequently enhances the signal-to-noise ratio (SNR)[42]. To assess the wavelength tolerance and suitability for telecom-band operation, we measured the responsivity of the PD across a broad wavelength range from 1490 nm to 1640 nm. At a wavelength of 1550 nm, the measured external responsivity is 0.21 A/

https://doi.org/10.1038/s41467-026-76733-8

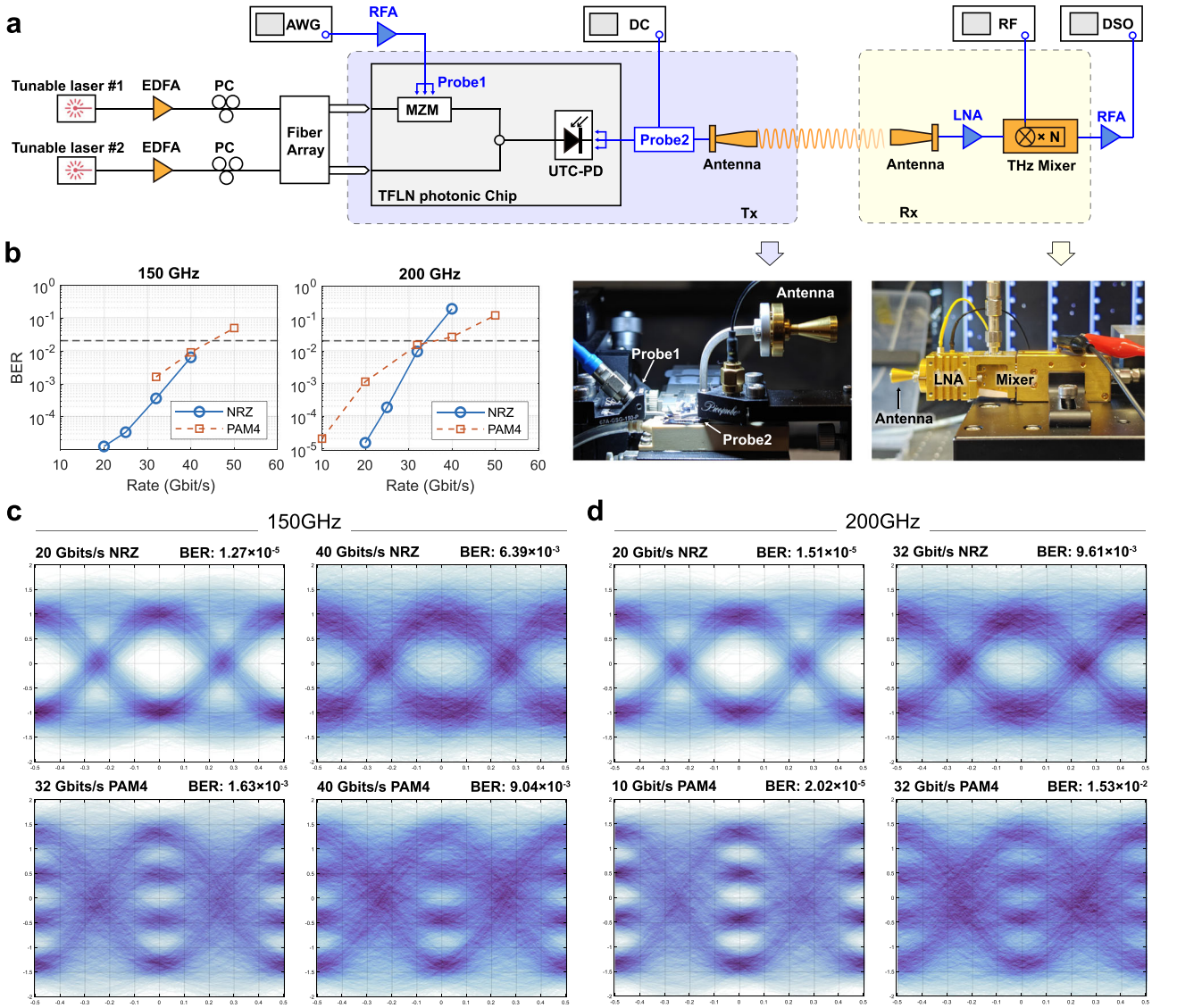


Fig. 4 | Proof-of-concept THz wireless data transmission. a Experimental setup of the THz wireless communication system. EDFA erbium-doped fiber amplifier, PC polarization controller, AWG arbitrary waveform generator, RFA radio frequency amplifier, MZM Mach-Zehnder modulator, UTC-PD uni-traveling carrier photodiode, DC DC source meter, LNA low-noise amplifier, DSO digital storage oscilloscope. The multiplication factor (N) of the THz mixer is 12 for 150 GHz and 16 for 200 GHz. The inserts: photographs of the integrated photonic transmitter during on-chip probing (left) and the receiver module (right). **b** Measured BER versus data rate for NRZ and PAM4 signals at 150 GHz and 200 GHz, with the dashed lines indicating the SD-FEC threshold. **c** Measured eye diagrams of the recovered NRZ (20 Gbit/s and 40 Gbit/s) and PAM4 (32 Gbit/s and 40 Gbit/s) signals at 150 GHz. **d** Measured eye diagrams of the recovered NRZ (20 Gbit/s and 32 Gbit/s) and PAM4 (10 Gbit/s and 32 Gbit/s) signals at 200 GHz.

W. By factoring in the measured −5 dB coupling loss between the lensed fiber and the TFLN waveguide facet, this yields a consistent internal responsivity of 0.67 A/W across multiple devices. Moreover, this internal responsivity shows a minimal variation of less than ±10% across the entire C+L-band, as shown in Fig. 3d. Such broadband optical absorption behavior facilitates flexible transmitter design and wavelength-division multiplexing (WDM) compatibility, allowing this UTC-PD to support multichannel or dynamically reconfigurable THz links.

THz wireless communication

A proof-of-concept experiment is conducted to validate wireless transmission enabled by the TFLN photonic integrated transmitter. As shown in Fig. 4a, two tunable lasers are amplified by Erbium-doped fiber amplifiers (EDFA) and coupled into the TFLN photonic chip via a fiber array. The on-chip TFLN modulator exhibits an EO 3-dB bandwidth exceeding 67 GHz (Fig. 3e) and a low half-wave voltage of 2.5 V. Driven by an arbitrary waveform generator (AWG) through an RF probe, the modulator is used to encode NRZ and PAM4 signals onto one of the optical carriers. The integrated UTC-PD then directly generates terahertz signals for wireless transmission, through heterodyne mixing between the two carriers. The THz output is delivered to a probe-contacted antenna without additional power amplifier, owing to the sufficient output power of the transmitter chip. The signal is received by an antenna after a 0.2 m wireless link, amplified by a frequency-matched low-noise amplifier (LNA), and down-converted to intermediate frequency (IF) with a corresponding subharmonic mixer driven by a frequency-multiplied Local Oscillator (specifically utilizing multiplication factors of ×12 and ×16 for the 150 GHz and 200 GHz bands, respectively). The specific LO is dynamically optimized to ensure the entire signal spectrum is captured by a real-time digital storage oscilloscope (DSO) and processed offline using digital signal processing (DSP) algorithms.

The transmission performance is summarized in Fig. 4b–d, with the photocurrent of the UTC-PD maintained at 1 mA. To validate the broadband capability of this transmitter, wireless communication experiments were conducted across a wide carrier frequency range from 120 GHz to 200 GHz. While the system demonstrates robust data transmission across the entire tested spectrum (detailed results for other frequency bands are provided in Supplementary Note 4), we focus our evaluation here on both NRZ and PAM4 modulation formats at representative carrier frequencies of 150 GHz and 200 GHz. As shown in Fig. 4b, the system achieves high-speed data transmission with BER remaining below the soft-decision forward error correction (SD-FEC) threshold. Notably, at 150 GHz, we achieve transmission rates up to 40 Gbit/s for both NRZ and PAM4 signals. Even at a carrier frequency of 200 GHz, the system robustly supports high-speed transmission of 32 Gbit/s for both modulation formats. Open eye diagrams are observed across these high data rates. Specifically, Fig. 4c illustrates the recovered NRZ and PAM4 eyes at 150 GHz, while Fig. 4d displays the recovered eyes at 200 GHz for both modulation formats. The gradual narrowing of the eyes with increasing baud rate is consistent with a reduced electrical SNR. Nevertheless, the achieved data rates show potential of compatibility with standards such as IEEE 802.15.3d, demonstrating the transmitter's applicability in multi-channel and multi-user scenarios. The achieved performance thus represents a conservative lower bound, with the integrated device's inherent bandwidth supporting significantly higher data rates. Overall, these results establish the feasibility of chip-scale THz wireless links using a heterogeneously integrated TFLN platform, while also indicating substantial headroom for further enhancement in both baud rate and carrier frequency.

Discussion

This work demonstrates a TFLN-based integrated THz photonic transmitter, in which a high-speed modulator is co-integrated with a heterogeneously bonded InP UTC-PD. System-level validation through high-speed wireless links using distinct modulation formats (NRZ and PAM4) at representative carrier frequencies of 150 GHz and 200 GHz confirms the functionality of this architecture. The demonstrated performance is enabled by the excellent EO performance of the TFLN platform and the integrated UTC-PD capability of operating in the THz regime. Table 1 summarizes the reported waveguide-based heterogeneously integrated high-speed PDs, showing that our device outperforms all previous demonstrations in 3-dB bandwidth, yielding the highest bandwidth-efficiency product to date. This advance arises from an optimized epitaxial design featuring a dual-step matching layer, which ensures efficient optical coupling while maintaining ultra-fast response.

At the system level, although dual-subcarrier modulation (DSC), where both optical tones are combined prior to simultaneous modulation, theoretically enhances the output power for basic intensity formats like NRZ[43], it introduces severe nonlinear distortions for multi-level signals. We therefore adopted the SSC architecture, which provides superior linearity, yields lower bit error rates for PAM4[43], and naturally scales to more complex, higher-order modulation formats.

Despite the achieved high-speed data transmission, the current system has not yet fully exploited the intrinsic capabilities of the >60 GHz modulator and the 240 GHz UTC-PD. From a practical link-design perspective, the overall transmission capacity is dictated by the complete end-to-end RF/THz signal path rather than the intrinsic bandwidth of the integrated photonic transmitter alone. As evaluated via multi-tone probing (detailed in Supplementary Note 5), this cascaded response suffers from frequency-dependent amplitude roll-offs and localized ripples induced by the modulator RF drive chain, THz probe-to-antenna coupling, subharmonic down-conversion, and LO multiplication. Furthermore, even with amplifiers integrated, the substantial free-space THz propagation loss of more than 60 dB over the 0.2 m wireless link significantly degrades the received signal-to-noise ratio. Consequently, these cascaded impairments collectively reduce the usable signal bandwidth and constrain the maximum achievable data rate. To overcome these limitations, future implementations can be optimized through hardware enhancements—such as employing flatter-gain broadband LNAs, lower-conversion-loss mixers, lower-loss waveguide transitions, and high-gain antennas—alongside calibrated RF pre-emphasis and high-efficiency digital signal processing (DSP) algorithms to equalize the residual link response. Building on these strategies, the proposed photonic transmitter architecture possesses the potential to scale towards kilometer-level THz wireless communications[44,45].

Building on this architecture, further enhancements in system capacity can also be realized through component-level improvements. On the modulator side, the TFLN platform enables I/Q modulation[46] for advanced modulation formats such as 16QAM and QPSK, as well as on-chip injection-locking schemes[47,48] that can enhance signal purity. On the PD side, refined optical-field engineering can improve the spatial uniformity of absorption without compromising responsivity. Advances in epitaxial design are expected to extend the operation to 300 GHz.

The demonstrated THz transmitter is highly compatible with other high-performance photonic components already realized on the TFLN platform, such as microcomb sources for phase-coherent carriers[49], optical true-time delay lines for THz beamforming[50]. In addition, heterogeneous laser integration on TFLN offers a pathway toward self-sufficient optical front ends[22,51], enabling fully monolithic transmitter architectures. Integrating these elements with the presented transmitter could yield comb-driven, multi-wavelength THz links featuring high integration density and multi-user connectivity, paving the way for practical deployment of compact, high-capacity wireless systems.

Table 1 | Comparison of III–V PDs heterogeneously integrated on different platforms

Year	PD/platform	Dark current (bias)	Responsivity (A/W)	f_{3dB} (GHz)	BEP (GHz·100%)	I_{sat} (mA)	$P_{sat,est.}$ (mW)
2023[24]	UTC on SiN	10 nA (−1 V)	0.30 (ext.)	155	37.2 (ext.)	4.6	15.33 (ext.)
2022[52]	MUTC on SiN/Si	30 nA (−3 V)	0.42 (1310 nm)	54	21.5	22	52.38
2016[53]	MUTC on Si	10 nA (−5 V)	0.64	48	24.6	N.A.	N.A.
2018[54]	MUTC on Si	1 nA (−3 V)	0.84	65	43.7	20	23.81
2022[55]	Lateral PIN on Si	0.06 nA (−1 V)	0.20	52	8.3	> 1	> 5
2022[30]	MUTC on TFLN	3 nA (−5 V)	0.60	80	38.4	N.A.	N.A.
2023[23]	MUTC on TFLN	1 nA (−4 V)	0.40	110	35.2	N.A.	N.A.
2025[31]	MUTC on TFLN	≤300 nA (−4 V)	0.40	140	44.8	N.A.	N.A.
This work	MUTC on TFLN	0.1 nA (−1 V)	0.67	240	128.7	2.8	4.18

BEP bandwidth-efficiency product, Ext. external value, *N.A.* not available, I_{sat} denotes the maximum or saturation photocurrent, $P_{sat,est}$ denotes the estimated incident optical power at saturation and is calculated from $P_{sat,\,est.} = I_{sat}/\mathcal{R}$, where $\mathcal{R}$ is the corresponding reported responsivity.

Methods

TFLN chip fabrication

Devices are fabricated on a commercially available x-cut TFLN wafer (NANOLN) consisting of a 500 nm LN, a 4.7 μm buried SiO_2 layer, and a 500 μm silicon substrate. A SiO_2 layer is first deposited on the TFLN wafer by plasma-enhanced chemical vapor deposition (PECVD) to serve as an etching hard mask. Optical waveguides and Mach-Zehnder interferometers (MZIs) are then patterned using UV stepper lithography, processed die by die (1.5 cm × 1.5 cm) with a resolution of 500 nm. The exposed photoresist patterns are subsequently transferred to the SiO_2 layer via a standard fluorine-based etching process and further into the LN layer using an optimized Ar-based inductively coupled plasma reactive-ion etching technique. The LN etch depth is ~250 nm, leaving a 250 nm thick slab. After removing the residual SiO_2 mask and redeposited materials, the wafer undergoes an annealing step. A sequence of second, third, and fourth lithography and lift-off processes is then performed to form the microwave electrodes, heater, and metal interconnects/pads, respectively. To enhance EO bandwidth, advanced slotted electrodes are implemented with a 5 μm slot length and 2 μm slot width. The positive and negative electrodes are separated by a 5 μm gap to ensure strong EO coupling while suppressing metal-induced optical loss.

Adhesive bonding and UTC-PD fabrication

After the patterning of the TFLN chip and EO modulater fabrication, III–V epitaxial dies were then bonded directly onto TFLN surface using an ultra-thin DVS-BCB adhesive process. Following the bonding process, Ti/Pt/Au layers were deposited to form p-contacts. The main MUTC structure was then patterned using a combination of ICP-RIE dry etching and wet etching (H_3PO_4:HCl = 3:1). Meanwhile, excess III–V material was removed to expose LN waveguides, ensuring low-loss propagation across the hybrid platform. Following the etching steps, GeAu/Ni/Au layers were deposited as n-contact metals, and a rapid thermal annealing process at 360 °C was conducted to ensure good ohmic contact. A 4 μm thick BCB layer was then applied to passivate the sidewalls of the MUTC structure and provide stable support for the subsequent electrodes made of Ti/Au layers. Detailed fabrication process flow can be found in the Supplementary Note 1.

RF measurements of the UTC-PD

The frequency response and saturation characteristics of the UTC-PD were examined using an optical heterodyne setup. Two tunable lasers were used to generate single-frequency beat signals covering a range from Megahertz to Terahertz. For frequencies ranging from DC to 110 GHz, the RF signal was captured with the Rohde & Schwarz power meter (NRP2) via a GSG Model 110H probe. For frequencies above 110 GHz, a VDI power meter (PM5B), together with a set of waveguide probes covering the 110-325 GHz range, was utilized to evaluate the generated terahertz power. The detailed schematics of two measurement setups can be found in Supplementary Note 3.

THz wireless communication setup

The experimental setup is shown in Fig. 4a. An arbitrary waveform generator is used for message loading with a sample rate of 92 GSa/s and a maximum effective bandwidth of 32 GHz. To optimize the optical mixing performance of the UTC-PD, the gains of the EDFAs are carefully adjusted to equalize the power of the optical LO and carrier, which is achieved by balancing the photocurrents generated by each optical tone incident to the UTC-PD. The photocurrent of the UTC-PD is maintained at 1 mA to avoid saturation and potential device damage. The generated THz signal is transmitted over a 0.2 m wireless link, corresponding to a total free-space path loss of 62.0 dB at 150 GHz and 64.5 dB at 200 GHz. The LNA matched to the specific operational bands are employed to compensate for the high loss of the terahertz signal across different tested carrier frequencies. Subsequently, the amplified signal is down-converted using a subharmonic THz mixer. As depicted by the multiplier block (×N) in Fig. 4a, a local oscillator multiplication factor of $N = 12$ is utilized for carrier frequencies up to 160 GHz, whereas $N = 16$ is utilized for the 200 GHz band characterization. The IF signal is captured by a DSO is used with a sample rate of 160 GSa/s and a maximum effective bandwidth of 59 GHz.

Digital signal processing procedure

The digital signal processing (DSP) procedure is structured as follows. At the transmitter, the source bit sequence is generated via offline digital signal processing (DSP) and directly mapped into corresponding NRZ and PAM4 symbols. Subsequently, pulse shaping and resampling are applied to effectively confine the signal bandwidth and match the sampling rate of the arbitrary waveform generator (AWG). Based on optimal testing, the roll-off factor is set to 0.6 for 20 GBaud and 25 GBaud signals, and 0.3 for all other symbol rates. At the receiver, initial timing recovery is performed using the Gardner algorithm to correct impairments from system components. Subsequently, feed-forward equalization (FFE) and decision feedback equalization (DFE) are applied to compensate for channel distortion. Specifically, the tap allocations are optimized according to the carrier frequencies and modulation formats: at 150 GHz, 80 FFE and 50 DFE taps are utilized for NRZ signals, while 70 FFE and 30 DFE taps are employed for PAM4 signals; at 200 GHz, 60 FFE and 30 DFE taps are applied for both modulation formats.

Data availability

The source data underlying the figures and findings generated in this study have been deposited in the Figshare database under 10.6084/m9.figshare.32946512 (https://doi.org/10.6084/m9.figshare.32946512).

References

1. Dang, S., Amin, O., Shihada, B. & Alouini, M.-S. What should 6G be?. *Nat. Electron.* **3**, 20–29 (2020).
2. Saad, W., Bennis, M. & Chen, M. A vision of 6G wireless systems: Applications, trends, technologies, and open research problems. *IEEE Netw.* **34**, 134–142 (2019).
3. Akyildiz, I. F., Han, C., Hu, Z., Nie, S. & Jornet, J. M. Terahertz band communication: an old problem revisited and research directions for the next decade. *IEEE Trans. Commun.* **70**, 4250–4285 (2022).
4. Chen, S. et al. Vision, requirements, and technology trend of 6G: how to tackle the challenges of system coverage, capacity, user data-rate and movement speed. *IEEE Wirel. Commun.* **27**, 218–228 (2020).
5. Song, H.-J. & Lee, N. Terahertz communications: challenges in the next decade. *IEEE Trans. Terahertz Sci. Technol.* **12**, 105–117 (2022).
6. Koenig, S. et al. Wireless sub-THz communication system with high data rate. *Nat. Photonics* **7**, 977–981 (2013).
7. Sengupta, K., Nagatsuma, T. & Mittleman, D. M. Terahertz integrated electronic and hybrid electronic-photonic systems. *Nat. Electron.* **1**, 622–635 (2018).
8. Montanaro, A. et al. Sub-THz wireless transmission based on graphene-integrated optoelectronic mixer. *Nat. Commun.* **14**, 6471 (2023).
9. Jia, S. et al. Integrated dual-laser photonic chip for high-purity carrier generation enabling ultrafast terahertz wireless communications. *Nat. Commun.* **13**, 1388 (2022).
10. Nagatsuma, T., Ducournau, G. & Renaud, C. C. Advances in terahertz communications accelerated by photonics. *Nat. Photonics* **10**, 371–379 (2016).
11. Seeds, A. J., Shams, H., Fice, M. J. & Renaud, C. C. TeraHertz photonics for wireless communications. *J. Lightwave Technol.* **33**, 579–587 (2015).
12. Ishibashi, T. & Ito, H. Uni-traveling-carrier photodiodes. *J. Appl. Phys.* **127**, 031101 (2020).
13. Ishibashi, T., Muramoto, Y., Yoshimatsu, T. & Ito, H. Unitraveling-carrier photodiodes for terahertz applications. *IEEE J. Sel. Top. Quantum Electron.* **20**, 79–88 (2014).

14. Ducournau, G. in *UTC-PD-Based Tx for Communications and Advanced Measurements* (ed.Kawanishi, T.) *Handbook of Radio and Optical Networks Convergence* 613–637 (Springer, 2024).
15. Nellen, S. et al. Experimental comparison of UTC- and PIN-photodiodes for continuous-wave terahertz generation. *J. Infrared Millim. Terahertz Waves* **41**, 343–354 (2020).
16. Li, L. et al. Modified uni-travelling-carrier photodiodes with 206 GHz bandwidth and 0.81 A W^{-1} external responsivity. *Nat. Photonics* **19**, 1301–1308 (2025).
17. Zhang, Y. et al. Integrated photonics enabling ultra-wideband fibre-wireless communication. *Nature* **651**, 348–355 (2026).
18. Rajabali, S. & Benea-Chelmus, I.-C. Present and future of terahertz integrated photonic devices. *APL Photonics* **8**, 080901 (2023).
19. García-Muñoz, E. et al. Photonic-based integrated sources and antenna arrays for broadband wireless links in terahertz communications. *Semicond. Sci. Technol.* **34**, 054001 (2019).
20. Smit, M. et al. An introduction to InP-based generic integration technology. *Semicond. Sci. Technol.* **29**, 083001 (2014).
21. Jacques, M. et al. Modulator material impact on chirp, DSP, and performance in coherent digital links: comparison of the lithium niobate, indium phosphide, and silicon platforms. *Opt. Express* **26**, 22471–22490 (2018).
22. Zhang, X. et al. Heterogeneously integrated III-V-on-lithium niobate broadband light sources and photodetectors. *Opt. Lett.* **47**, 4564 (2022).
23. Wei, C. et al. Ultra-wideband waveguide-coupled photodiodes heterogeneously integrated on a thin-film lithium niobate platform. *Light Adv. Manuf.* **4**, 1 (2023).
24. Maes, D. et al. High-speed uni-traveling-carrier photodiodes on silicon nitride. *APL Photonics* **8**, 016104 (2023).
25. Wang, C. et al. Integrated lithium niobate electro-optic modulators operating at CMOS-compatible voltages. *Nature* **562**, 101–104 (2018).
26. Feng, H. et al. On-chip optical vector analysis based on thin-film lithium niobate single-sideband modulators. *Adv. Photonics* **6**, 066006 (2024).
27. Tao, Z. et al. Ultrabroadband on-chip photonics for full-spectrum wireless communications. *Nature* **645**, 80–87 (2025).
28. Feng, H. et al. Integrated lithium niobate microwave photonic processing engine. *Nature* **627**, 80–87 (2024).
29. Wei, C. et al. Programmable multifunctional integrated microwave photonic circuit on thin-film lithium niobate. *Nat. Commun.* **16**, 2281 (2025).
30. Guo, X. et al. High-performance modified uni-traveling carrier photodiode integrated on a thin-film lithium niobate platform. *Photonics Res.* **10**, 1338 (2022).
31. Xie, X. et al. A 3.584 Tbps coherent receiver chip on InP-$LiNbO_3$ wafer-level integration platform. *Light.: Sci. Appl.* **14**, 172 (2025).
32. Beckerwerth, T., Runge, P. & Schell, M. High-speed photodiodes for power efficient data transmission. *J. Lightwave Technol.* **42**, 1056–1061 (2023).
33. Chaccour, C., Soorki, M. N., Saad, W., Bennis, M. & Popovski, P. Can terahertz provide high-rate reliable low-latency communications for wireless VR?. *IEEE Internet Things J.* **9**, 9712–9729 (2022).
34. Zugno, T. et al. Use cases for terahertz communications: an industrial perspective. *IEEE Wirel. Commun.* **32**, 90–98 (2025).
35. Jiang, C., Yin, Y., Yin, X. & Hao, Q. Short Range and High Speed Terahertz Wireless Interconnect Technology for Data Centers. *5th International Seminar on Artifi cial Intelligence*, 1823–1826 (Networking and Information Technology (AINIT), 2024).
36. Gong, T. et al. Holographic MIMO communications: theoretical foundations, enabling technologies, and future directions. *IEEE Commun. Surv. Tutor.* **26**, 196–257 (2024).
37. Mineeva, V. et al. A novel feature-oriented quality of anything (QoX) framework for end-to-end robotic services in 6G networks. *Sci. Rep.* **15**, 24945 (2025).
38. Keyvaninia, S. et al. Ultra-thin DVS-BCB adhesive bonding of III-V wafers, dies and multiple dies to a patterned silicon-on-insulator substrate. *Optical Mater. Express* **3**, 35 (2013).
39. Li, L. et al. Ultra-fast waveguide MUTC photodiodes over 220 GHz. *J. Lightwave Technol.* **42**, 7451–7457 (2024).
40. Ito, H. et al. Over-10-dBm output uni-traveling-carrier photodiode module integrating a power amplifier for wireless transmissions in the 125-GHz band. *IEICE Electron. Express* **2**, 446–450 (2005).
41. Shrestha, R., Guerboukha, H., Fang, Z., Knightly, E. & Mittleman, D. M. Jamming a terahertz wireless link. *Nat. Commun.* **13**, 3045 (2022).
42. Dardano, P. & Ferrara, M. A. Integrated photodetectors based on group IV and colloidal semiconductors: current state of affairs. *Micromachines* **11**, 842 (2020).
43. Gonzalez-Guerrero, L., Ali, M., Guzman, R., Lamela, H. & Carpintero, G. Photonic sub-terahertz IM links: comparison between double and single carrier modulation. *J. Lightwave Technol.* **40**, 6064–6070 (2022).
44. Lyu, Z. et al. *Field Trial on Photonic THz Real-Time Transmission of 50Gbit/s over 1km Wireless Link*, PDP_6 (Optica Publishing Group, 2024).
45. Liu, K. et al. High-speed 0.22 THz communication system with 84 Gbps for real-time uncompressed 8K video transmission of live events. *Nat. Commun.* **15**, 8037 (2024).
46. Xu, M. et al. High-performance coherent optical modulators based on thin-film lithium niobate platform. *Nat. Commun.* **11**, 3911 (2020).
47. Han, M. et al. Integrated self-injection-locked narrow linewidth laser based on thin-film lithium niobate. *Opt. Express* **32**, 5632 (2024).
48. Wan, S. et al. Self-locked broadband Raman-electro-optic microcomb. *Nat. Commun.* **16**, 4829 (2025).
49. Xie, X. et al. Broadband millimeter-wave frequency mixer based on thin-film lithium niobate photonics. *Electromagn. Sci.* **3**, 0090462–1 (2025).
50. Qin, Y. et al. Broadband lithium niobate integrated microwave photonic beamforming chip. *Laser Photonics Rev.* **19**, e00219 (2025).
51. Shams-Ansari, A. et al. Electrically pumped laser transmitter integrated on thin-film lithium niobate. *Optica* **9**, 408 (2022).
52. Yu, F. et al. High-power high-speed MUTC waveguide photodiodes integrated on Si_3N_4/Si platform using micro-transfer printing. *IEEE J. Sel. Top. Quantum Electron.* **29**, 1–6 (2022).
53. Xie, X. et al. High-power and high-speed heterogeneously integrated waveguide-coupled photodiodes on silicon-on-insulator. *J. Lightwave Technol.* **34**, 73–78 (2016).
54. Wang, Y. et al. High-power photodiodes with 65 GHz bandwidth heterogeneously integrated onto silicon-on-insulator nano-waveguides. *IEEE J. Sel. Top. Quantum Electron.* **24**, 1–6 (2018).
55. Xue, Y. et al. High-speed and low dark current silicon-waveguide-coupled III-V photodetectors selectively grown on SOI. *Optica* **9**, 1219 (2022).

Acknowledgements

The PD chips were fabricated with support from the ShanghaiTech Material and Device Lab (SMDL). We thank W. H. Wong at CityU for the help in device fabrication. We thank the technical support of C. F. Yeung, C. W. Lai and L. Ho at HKUST, Nanosystem Fabrication Facility (NFF), for the stepper lithography and PECVD process.

Author contributions

B. Chen conceived the idea. L. Wang, Z. Zhang, and B. Chen designed the UTC PD structure. H. Feng, Y. Wu and C. Wang designed the TFLN device. L. Wang, H. Feng, Z. Zhang, Y. Wu, L. Li, D. Gu and T. Long jointly fabricated the devices and participated in the testing process. L. Wang,

L. Bai and Z. Ding conducted the terahertz communication experiment supervised by Z. Lyu, X. Yu, L. Zhang and B. Chen. L. Wang, H. Feng, L.Bai, Z. Zhang, Z. Lyu, L. Zhang, C. Wang and B. Chen primarily wrote the manuscript. B. Chen, C. Wang and Z. Lyu supervised the project.

Funding

B.C. acknowledges support from the National Key Research and Development Program of China (2018YFB2201000), the National Natural Science Foundation of China (61975121), National Key Laboratory of Infrared Detection Technologies of China (IRDT-ZGKXY-25-12) and ShanghaiTech AI Initiative (AI2026A05). H.F. acknowledges support from the Research Grants Council, University Grants Committee (JRFS2526-1S01), Guangdong and Hong Kong Universities '1+1+1' Joint Research Collaboration Scheme. C.W. acknowledges support from the Research Grants Council, University Grants Committee (STG3_E-104_25-N, C1002-22Y, STG3/E-704/23-N, CityU 11204022, CityU 11204523) and the Croucher Foundation (9509005).

Competing interests

The authors declare no competing interests.

Additional information

Supplementary information The online version contains supplementary material available at https://doi.org/10.1038/s41467-026-76733-8.

Correspondence and requests for materials should be addressed to Zhidong Lyu, Cheng Wang or Baile Chen.

Peer review information *Nature Communications* thanks Ileana-Cristina Benea-Chelmus and the other anonymous reviewer(s) for their contribution to the peer review of this work. A peer review file is available.

Reprints and permissions information is available at http://www.nature.com/reprints

Publisher's note Springer Nature remains neutral with regard to jurisdictional claims in published maps and institutional affiliations.

Open Access This article is licensed under a Creative Commons Attribution-NonCommercial-NoDerivatives 4.0 International License, which permits any non-commercial use, sharing, distribution and reproduction in any medium or format, as long as you give appropriate credit to the original author(s) and the source, provide a link to the Creative Commons licence, and indicate if you modified the licensed material. You do not have permission under this licence to share adapted material derived from this article or parts of it. The images or other third party material in this article are included in the article's Creative Commons licence, unless indicated otherwise in a credit line to the material. If material is not included in the article's Creative Commons licence and your intended use is not permitted by statutory regulation or exceeds the permitted use, you will need to obtain permission directly from the copyright holder. To view a copy of this licence, visit http://creativecommons.org/licenses/by-nc-nd/4.0/.

© The Author(s) 2026